Biophysical study of resin acid effects on phospholipid membrane 1 structure and properties

Jagalski, Vivian; Barker, Robert; Topgaard, Daniel; Günther Pomorski, Thomas; Hamberger, Björn; Cárdenas, Marité

Published in:
BBA - Biomembranes

DOI:
10.1016/j.bbamem.2016.08.008

Publication date:
2016

Biophysical study of resin acid effects on phospholipid membrane structure and properties

Vivien Jagalski[1], Robert Barker[2], Daniel Topgaard[3], Thomas Günther Pomorski[4], Björn Hamberger[4], Marité Cárdenas[5,1]

[1] *Nano Science Center and Department of Chemistry, University of Copenhagen, Copenhagen, Denmark.*
[2] *Institute Laue Langevin, 71 avenue de Matyrs, CS 20156, 38042 Grenoble Cedex 9, France. Current address: School of Science and Engineering, University of Dundee, Dundee DD1 4HN, United Kingdom.*
[3]*Division of Physical Chemistry, Chemistry Department, Lund University, Sweden*
[4]*Department of Plant and Environmental Sciences, University of Copenhagen, Copenhagen, Denmark.*
[5]*Biofilm – Research center for Biointerfaces and Department of Biomedical Science, Malmö University, Malmö, Sweden.*

Abstract

Hydrophobic resin acids (RAs) are synthesized by trees as part of their defence mechanisms. One of the functions of RAs in plant defence is suggested to be the perturbation of the cellular membrane. However, there is vast diversity of chemical structure within this class of molecules, and there are no clear correlations to the molecular mechanisms behind the RA's toxicity. In this study we unravel the molecular interactions of three closely related RAs dehydroabietic acid, neoabietic acid, and the synthetic analogue dichlorodehydroabietic acid with dipalmitoylphosphatidylcholine (DPPC) model membranes and the polar lipid extract of soybeans. The complementarity of the biophysical techniques used (PT ssNMR, DLS, NR, DSC, Cryo-TEM) allowed correlating changes at the vesicle level with changes at the molecular level and the co-localization of RAs within DPPC monolayer. Effects on DPPC membranes are correlated with the physical chemical properties of the RA and their toxicity.

1. Introduction

Resin acids (RAs) belong to an important class of natural biologically active compounds that form part of the defence mechanisms of certain plants, e.g. conifer trees [1]. Today they are widely applied as natural insecticides and have potential use in new industrial applications due to their antimicrobial and antifungal properties [2].

RAs are tricyclic diterpenes of the labdane type, which derive from the precursor geranylgeranyl diphosphate (GGPP), consist of 20 carbon atoms and carry a carboxyl group. Their high chemical diversity arises from various functional groups, diastereoisomers and the number and position of double bonds [1]. In order to circumvent toxic effects, the synthesis of natural RAs, e.g. in pines, takes place in specialized epithelial cells after which they are concentrated and stored in cell free resin ducts [3]. Additionally, a wide range of synthetic and modified RAs exist today, such as dichlorodehydroabietic acid (Cl_2DAA) schematically shown in Fig. 1. Cl_2DAA is a waste product from bleaching processes in paper mills and pulp effluents and is highly toxic for aquatic organisms [4].

The toxicity of RAs against insects, fungi and other organisms is currently linked to their ability to integrate into the cellular membrane due to their hydrophobicity. The concentrated release of RAs toward an invading organism or upon tissue damage is suggested to locally induce a toxic RA to lipid ratio. In particular, toxicological studies showed that RAs' toxicity correlates to the perturbation of the cellular membrane integrity. Electron paramagnetic resonance was used for *in vitro* assays to study the cytotoxicity of terpenes on erythrocytes showing a clear weakening of the cell membrane upon exposure to terpenes closely related to the RAs used in this study [5]. Biophysical studies also showed that terpenes, such as abietic acid from the oleo resin, increase both the permeability and fluidity of the cellular membrane suggesting a more disordered lipid packing in DPPC and DMPC bilayers [6, 7].

It is noteworthy that small structural differences in terpenes (for example, a single bond in *cis* or *trans* conformation or additional functional groups) can lead to major differences in toxicity that may correlate to their degree of lipid membrane perturbance [8]. However, no systematic studies investigating the structural effects of RAs on model phospholipid monolayers and bilayers have been reported to date.

Here, we study the lipid membrane structure and morphology using both DPPC and soybean polar lipid extract in admixture with 3 RAs of similar chemical structure, namely natural dehydroabietic

acid (DAA) and neoabietic acid (NA), both found in conifer resin, as well as their synthetic analogue (Cl_2DAA). Toxicological studies concluded that among natural compounds DAA has a higher antimicrobial toxicity than NA [9], while another study (that included Cl_2DAA and DAA) reported a significantly higher toxicity of chlorinated compounds over non-chlorinated compounds [10]. The chemical structures of the three RAs and the main phospholipid DPPC used in this study are shown in Fig. 1.

Fig. 1. Molecular structures of the three diterpene resin acids (RAs) and the lipid used in this study. Top, from the left: dichlorodehydroabietic acid (Cl_2DAA), dehydroabietic acid (DAA) and neoabietic acid (NA). Bottom: the chemical structure of the main lipid used in this study, Dipalmitoylphosphatidylcholine (DPPC) including the carbon numbering relevant for the PT ssNMR analysis.

Specifically, we investigated the effect of RAs on the biophysical properties and structure of both lipid vesicles and lipid monolayers using a wide range of complementary biophysical techniques. Differential scanning calorimetry (DSC), polarization transfer solid-state nuclear magnetic resonance (PT ssNMR), dynamic light scattering (DLS) and cryogenic transmission electron microscopy (Cryo-TEM) were used to reveal the overall structural effects on DPPC bilayers. Neutron reflectometry (NR) and the Langmuir trough (LT) were used to investigate changes at the molecular level and the RAs´ localization within the lipid monolayer. The complementarity of these techniques allowed correlating changes at the vesicle level with changes at the molecular level of DPPC membranes in the presence of RAs. Additionally, the DLS measurements of polar soy lipid extract suggest that the effects observed for DPPC also apply to more biologically relevant lipid mixtures.

2. Experimental Section

2.1 Materials

The lipids, DPPC, 1,2-dipalmitoyl-d62-*sn*-glycero-3-phosphocholine (d_{62}DPPC), 1,2-dipalmitoyl-*sn*-glycero-3-phosphocholine-N,N,N-trimethyl-d9 (d_9DPPC) and soybean polar lipid extract (Composition in wt/wt%: phosphatidylcholine: 45.7, phosphatidylethanolamine: 22.1, phosphoinositol: 18.4, phosphatidic acid: 6.9 and unknown: 6.9) [11] were purchased from Avanti Polar Lipids, Inc. (AL, USA) with a purity over 99 %. Tris-buffered saline (TBS) solution containing 50 mM Tris and 150 mM NaCl at pH of 7.4 was used in all preparations. Cl_2DAA, DAA

and NA were purchased from Orchid, Cellmark (Canada). All other chemicals were obtained from Sigma Aldrich (Brøndby, Denmark) unless otherwise indicated.

2.1. Vesicle Preparation

Vesicles were prepared by manual extrusion. Briefly, lipids and RAs dissolved in chloroform were mixed at a molar ratio of 9:1 and spread onto the glass vial surface with a glass syringe (Hamilton, USA), followed by drying under a soft nitrogen stream and subjection for 1 hour under a vacuum to remove residual organic solvent. Lipid films were used immediately or stored at -20°C. The lipid film was rehydrated and extruded in buffer well above the melting temperature (T_m), which is reported to be 41°C for DPPC [12] and -63°C [13] for soybean polar lipids. The vesicle suspension was extruded eleven times through a 100 nm pore size polycarbonate filter membrane using a mini extruder (Avanti Polar Lipids, Inc.).

2.2. Dynamic Light Scattering (DLS)

DLS measurements were performed using an ALV/CGS-3 (ALV- GmbH, Germany) apparatus containing a Helium-Neon Laser (λ =632.8 nm) to determine the hydrodynamic size of the vesicle population. The experiment was performed in TBS buffer at a final vesicle concentration of 0.1 mg lipid/ml. Measurements for each sample were taken out immediately after extrusion (h_0) and one day later (h_{24}). Data was collected at a detection angle of θ = 90° for 60 seconds. The data was analyzed with the ALV correlator Software 3.0 (ALV GmbH, Germany).

For the analysis, the normalized electric field correlation ($g_1(t)$), which describes the measured intensity fluctuations, is determined by using the distribution of exponential decays

$$g_1(t) = \int A(\tau) \exp(-t/\tau) d\tau$$

where τ is the relaxation time and A(τ) its distribution. Therefore, the contribution of a particle to A(τ) is proportional to its scattering intensity and thus large particles bias strongly the distribution. Furthermore, the cooperative diffusion coefficient (D_c) relates to τ via the relationship

$$\tau = (D_c q^2)^{-1}$$

with q as the scattering vector ($q = 4\pi n/\lambda \sin(\theta/2)$). At an infinite dilution D_c will be reduced to the self-diffusion coefficient of the particle in solution and therefore links to the hydrodynamic radius which is calculated by the Stokes- Einstein equation

$$D = \frac{kT}{6\pi\eta R}$$

with T as the temperature in Kelvin, k being the Boltzmann Constant, R as the hydrodynamic radius, the solution viscosity (η = 0.89 mPa s) as well as the refractive index of water (n = 1.33) [14][15]. The DLS data is displayed as relaxation time distributions vs the hydrodynamic radii (nm).

2.3. Cryogenic-Transmission Electron Microscopy (cryo-TEM)

Cryo-TEM was applied to visualize the shape and size of the vesicles and aggregates. The imaging was performed with a Philips CM120 BioTWIN microscope (University of Lund, Sweden) with an Oxford CT 3500 Cryoholder and transfer system. This instrument gives a high resolution down to 0.34 nm [16]. Solutions with a final vesicle concentration of 1 mg/ml in TBS were prepared one day prior to the experiment. The samples were prepared by plunge freezing. Briefly, a small drop of the vesicle solution was transferred to a thin carbon grid and after gently removing the excess liquid, the sample was rapidly frozen at -180°C in an ethane bath. During both, the transfer and the imaging the samples were kept at -150°C using liquid nitrogen. At least 330 vesicles in two replicates generated from one aliquot were analyzed with the Software ImageJ (National institute of Health, Maryland, USA) to measure the average diameter without further image treatment.

2.4. Surface pressure - area (π-A) isotherms at the air/water interface

Surface Pressure – area (π-A) isotherms were undertaken at the air/water interface on a mini trough film balance (KSV Instruments Ldt., Finland) with a working surface area of 144 cm^2. The water surface was considered to be clean after a total area compression did not lead to a change in surface pressure of more than 0.1 mN/m, and the measured π was that of water at 25°C (72 mN/m) [17]. The lipids and RAs were mixed in chloroform prior use and spread on the water surface to reach a mean molecular area (MMA) of ~128 $Å^2$ for each mixture. The chloroform solution was given 15 minutes to evaporate before the π-A isotherms were measured with a compression speed of 1 cm per minute at constant temperature. The temperature was controlled with an external water bath. To

additionally analyze changes in compressibility of the lipids the compressibility modulus (C_s^{-1}) was calculated using the formula

$$C_s^{-1} = -A\left[\frac{\partial \pi}{\partial A}\right]$$

in which π is the surface pressure and A is the MMA at a given point.

2.5 Neutron Reflectometry (NR)

Specular neutron reflectometry (NR) was used to analyze the structure of DPPC/RA monolayers at the air/water interface. NR enables one to obtain structural information perpendicular to the interface in a non-destructive manner. Two reflectometers were used in this study: FIGARO at the Institute Laue-Langevin (Grenoble, France) [18] and INTER at the Rutherford Appleton Laboratories (Didcot, UK) [19] Briefly, an incident "white" neutron beam, with a chosen wavelength (λ) generated by a single crystal monochromator, is directed on the air/water interface and is partially reflected and refracted depending on the incident angle (θ) and λ. The ratio between incident and reflected beam is then measured as a function of the wave vector defined as $Q = \frac{4\pi}{\lambda}\sin\theta$. To obtain detailed structural information the isotropic contrast in the sample is important. The scattering length density (SLD) determines the isotropic contrast by highlighting different components in the sample. The SLD is described by the sum of the coherent scattering length b_j times the number of nuclei in a given volume n_j ($SLD = \sum n_j \times b_j$). By exchanging hydrogen with deuterium, the SLD of a molecule can be increased and the isotropic contrast can be manipulated to partially highlight specific parts of a molecule. In this study, the four isotropic contrasts consisted of $_{d62}$DPPC on D_2O, $_{d62}$DPPC on air contrast matching water (ACMW, 8 w% D_2O), hDPPC on D_2O and $_{d9}$DPPC on ACMW with and without the presence of RA.

For these experiments, a Langmuir trough with two movable barriers and a total compressible area of 605.3 cm^2 was used. The experiments were performed under the same conditions as stated for the π - A isotherms section, adjusted to the larger trough area respectively The measurements were carried out at π = 30 mN/m, which is the estimated lateral pressure of a biological membrane [20]. In the data interpretation procedure, the four isotropic contrasts were simultaneously fitted to get a unique model. The data was analyzed using the Motofit software, which uses the Abeles matrix for

simulations of reflectometry data [21]. The SLD values used in the fitting procedure are summarized in table Supporting Information SI 2. Briefly, a two-layer model was applied that separates the head group from the acyl chain region of the monolayer. Each layer was given a specific SLD. In this way, we determined the thickness and roughness of each layer as well as the solvent penetration into the head group. The roughness of each layer was larger or equal to the roughness induced by capillary forces 3.7Å (Supporting Information Fig. 1). Specifically, from the fitted parameters the hydration ($\emptyset p$ of the head group was calculated using the following relationship:

$$SLD_{head\ group} = (Layer_{SLD\ ideal} \times (1 - \emptyset)) + Bulk_{SLD} \times \emptyset)$$

2.6 Differential Scanning Calorimetry (DSC)

DSC experiments were performed using a MicroCal™ VP-DSC system (GE Healthcare Bio-Sciences, Sweden). Extruded vesicles (1 mg lipid /ml in TBS) were measured in two thermal cycles including heating and cooling from 10 to 70°C at a rate of 1°C per 1.5 minutes and a chamber filled with buffer as a reference. Duplicates were analyzed on the VPViewerTM2000 (GE Healthcare, MA, USA) software. The enthalpy (ΔH°) of the $L_{\beta'} - L_{\alpha}$ phase transition was determined by the area below the main phase-transition peak of a heating cycle. Additionally, the cooperative unit (CU) was calculated using the van't Hoff enthalpy (ΔH_{vH}) for a two state model based on the assumption that no significant intermediate populations occur [22]. ΔH_{vH} is calculated using the following relationship:

$$\frac{\partial \ln K}{\partial T} = \frac{\Delta H}{\Delta H_{vH} R T^2}$$

where K is the equilibrium constant of the $L_{\beta'} - L_{\alpha}$ phase transition, R is the gas constant, T is the absolute Temperature (Kelvin), and ΔH_{vH} is the van´t Hoff enthalpy. CU is then defined by the ratio of the transition enthalpy and the van´t Hoff enthalpy ($\Delta H_{vH}/\Delta H_{cal}$) and displays the amount of molecules within one cooperative unit [23].

2.7 Polarization transfer solid-state nuclear magnetic resonance (PT ssNMR)

For the PT ssNMR studies, 20 mg of fully hydrated DPPC, DPPC/DAA and DPPC/NA samples at a water to lipid molar ratio of 40:1 were prepared 21 days before the measurement to ensure sufficient equilibration time. The lipid samples were prepared using TBS buffer and loaded into rotor inserts that were then placed in a 4 mm Bruker rotor.

NMR experiments were performed at ^{1}H and ^{13}C resonance frequencies of, respectively, 500 and 125 MHz on a Bruker Avance II 500 spectrometer with a 4 mm $^{13}C/^{31}P/^{1}H$ Efree probe. The ^{13}C signal was recorded under 5 kHz magic-angle spinning (MAS) [24] and 48 kHz two pulse phase modulation (TPPM) decoupling [25] with 31.25 kHz spectral width and 100 ms acquisition time. The ^{13}C chemical shift was referenced to tetramethylsilane using the 43.67 ppm a-carbon signal of a-glycine as secondary standard [26]. Hard radiofrequency (RF) pulses were applied at 80 kHz nutation frequency, giving 90° and 180° pulse lengths of, respectively, 3.1 and 6.2 ms. Direct polarization (DP) spectra were acquired after a single ^{13}C 90° pulse. Selective enhancement of resonances from rigid and mobile segments were achieved by the cross polarization (CP) [27] and insensitive nuclei enhanced by polarization transfer (INEPT) [28] schemes. CP was carried out with 1 ms contact time, 80 kHz ^{13}C nutation frequency, and linear ramp of ^{1}H nutation frequency from 72 to 88 kHz. The INEPT measurements were performed with the delays t = 1.2 ms and t' = 1.8 ms. Each spectrum was acquired by accumulating 256 transients at 5 s recycle delay. The sample temperature was controlled with a Bruker BVT unit and calibrated to an accuracy of 0.2°C with methanol at 5 kHz MAS [29].

The data was processed with 20 Hz line broadening, zero-filling from 1560 to 8192 points, Fourier transformation, automatic phase correction [30], and baseline correction using in-house Matlab scripts based on matNMR [31]. In order to facilitate observation of transitions between solid and liquid phases, the DP, CP, and INEPT spectra were overlaid and color-coded in gray, blue, and red, respectively [32,33]. This set of measurements is known under the term polarization transfer solid-state NMR (PT ssNMR) and has been applied for studies of phase transitions in a wide range of aqueous surfactant and lipid systems [33–36].

3. Results

3.1. Formation of large vesicular structures in the presence of RAs

DLS and Cryo-TEM were combined to characterize the vesicle size and shape distribution in samples based on either DPPC or the polar soybean lipid extract with and without 10 mol% RA. Freshly extruded vesicles and vesicles incubated for 24 h at room temperature (RT) after extrusion were measured with DLS at 90° (Fig. 2 and Supporting Information Fig. S2 and S3). For DPPC alone, a monodisperse vesicle population with an average radius of 70 ± 4 nm (n=3) with a stable size distribution over at least 24 h was observed. For polar soybean lipid vesicles, the mean vesicle size was 40 ± 10 nm both right after extrusion (h_0) and after 24 h of incubation at RT (h_{24}). However, the size distribution broadened towards larger vesicles over time (Supporting Information S2) reflecting higher dynamics of the polar soybean lipid extract due to their higher fluidity as compared to the more static gel phase DPPC vesicles. Due to these differences, Fig. 2 shows the DLS data for soy lipid/RA mixtures at h_0, whereas the DPPC/RA mixtures are presented at h_{24} to allow for a longer equilibration time and similar extent of mixing for both lipid systems. The h_0 and h_{24} data sets for DPPC/RA and soybean lipid/RA mixtures are given in Supporting Information Fig. S3.

For DPPC vesicles, the presence of RAs led to a broadening and shifting of the vesicle peak maximum towards smaller sizes already at h_0 (Supporting Information Fig. S3). Over time (h_{24}) this vesicle population was accompanied by the appearance of a second maximum for Cl_2DAA and DAA at larger vesicle sizes (Fig. 2A). For DPPC/Cl_2DAA, the first maximum appeared at 70 ± 5 nm and a second maximum appeared at 290 ± 60 nm. When DAA was added, the first maximum occurred at 50 ± 10 nm and either a long tail or a second smaller peak appeared at 380 ± 60 nm. For DPPC/NA vesicles, the maximum in size distribution shifted also to slightly smaller radii (60 ± 3 nm) at the same time that the peak broadened toward larger vesicles with a maximum radius of ~130 nm. Additionally, the DLS detector-counts for a given laser opening remained roughly constant suggesting that very large aggregates that sediment did not accumulate in DPPC samples.

Fig.2. Impact of resin acids on lipid vesicles prepared from DPPC after 24 hours of incubation at RT (A) and the polar soy lipid extract immediately after extrusion (B) without (solid line) and with (dotted lines) a given RA (10 mol %). In this figure $\tau A(\tau)$ is plotted as a function of the hydrodynamic size radius (nm) showing qualitatively the appearance of larger vesicular structures in the presence of RAs.

When RAs were added to polar soybean lipid vesicles, a similar effect was observed at h_0 (Fig. 2B). Specifically, two maxima were observed at radii of 50 ± 20 nm and 70 ± 10 nm when Cl_2DAA was incorporated into soybean lipid vesicles. For soybean/DAA vesicles, the maximum in the size distribution occurred at 40 ± 10 nm and a long tail appeared at higher sizes up to 160 ± 30 nm. For soybean/NA lipid vesicles, the broadening of the size distribution was also accompanied by a significant shift in the maximum of the observed vesicle size to 60 ± 10 nm. The soybean lipid extract vesicles tend to aggregate over time and thus these differences are less clear at h_{24} (Supporting Information Fig. S2). To sum up, for both DPPC and the polar soybean lipid extract two of the three RAs lead to the formation of larger vesicular structures suggesting similar structural effects for the model DPPC/RA, as well as for the more biologically relevant soybean/RA mixture.

Fig. 3. A) Cryo TEM images of DPPC vesicles in the presence of 10 mol% RA: DPPC (1) with 10 mol%, NA (2), Cl_2DAA (3) and DAA (4). B) Correlating histograms of maximum vesicle lengths (nm) that were obtained from 330 distinct vesicles.

To analyze the reasons behind the increase in vesicle size on the microscopic level, DPPC/RA vesicles were visualized by Cryo-TEM (Fig. 3A). DPPC vesicles presented rhombic (faceted) shapes typical for lipid vesicles in the gel phase [37]**.** The majority of vesicles were unilamellar with a quite narrow size distribution, as expected due to the extrusion. For DPPC/RA mixtures, spherical rhombic vesicles were accompanied by smooth tubular structures, which were mainly found in clusters. To quantify the impact on the length, the maximum diameters of 330 individual vesicles were measured and the histograms of the corresponding lengths are shown in Fig. 3B. The vesicle size distribution obtained using Cryo-TEM imaging for DPPC vesicles gave a radius of 47 ± 17 nm (Fig. 3B and Fig. 2A). The majority of vesicles in all samples show a maximum diameter at ~110 nm and furthermore no DPPC vesicles larger than 250 nm occurred in the absence of RAs (Fig. 3B). Therefore, all tubular structures with a maximum diameter over 250 nm must be induced by RAs. The addition of Cl_2DAA and DAA produced tubular vesicles with a maximum length of 830 nm and 860 nm, respectively. The percentage of vesicle structures above a 250 nm length for Cl_2DAA was 21%, while that value was 11% and 3% for DAA and NA, respectively. Clearly, the overall size and structure of most vesicles remained unaffected by RAs. The Cryo-TEM-based size

distribution (Fig. 3B) is qualitatively consistent with that produced by DLS (Fig. 2A) and the presence of larger vesicular structures follows the trend Cl_2DAA > DAA > NA. The main differences in absolute sizes and relative intensities presented from DLS and Cryo-TEM depend on the physical basis of the techniques used, as DLS measures the size dependent scattering intensities in bulk solution, while Cryo-TEM allows the evaluation at the single vesicle level.

3.2. Decreased lipid compressibility in the presence of RAs

The RA effect on lipid packing in DPPC monolayers was studied using Langmuir (π-A) isotherms (Fig. 4A). Briefly, the DPPC molecules were added onto the aqueous subphase in the gaseous phase at $\pi = 0$. As π increased, the monolayer underwent a phase transition into the liquid- expanded (LE) phase up to $\pi \sim 10$ mN. Then a first order phase transition to the liquid - condensed (LC) phase took place, during which the LE and LC phases co-existed. The isotherm for DPPC is similar to that reported earlier under similar experimental conditions [38-39].

Fig. 4. Impact of RAs on lipid packing in monolayers. A) π - MMA isotherms for DPPC and DPPC/RA (9:1 molar ratio) monolayers on water. B) Compressibility modulus plot (C_s^{-1}) versus surface pressure displaying the compressibility of the mixtures at all points during compression. The liquid expanded (LE) and liquid condensed (LC) phases are labelled in B for clarity.

In the presence of RAs, the π-A isotherm of DPPC monolayers shifted to smaller MMA as compared to the control regardless of the RA type (Fig. 4A). The shift towards smaller MMA depended on the RA type following the trend: Cl_2DAA > NA > DAA. We cannot rule out a loss of the molecules into the bulk aqueous solution, e.g. in form of mixed lipid/RA micelles, and therefore we do not further analyze this apparent compaction. However, the slope of the isotherms in the LC region changed upon RA addition suggesting changes in compressibility. Indeed, C_s^{-1} decreased in the LC- phase over $\pi = 15$ mN/m while the minimum of C_s^{-1} shifted slightly to a higher surface pressure for all RAs for DPPC-RA mixtures (Fig. 4B). Overall, our data suggests that RAs integrate within the phospholipid monolayer inducing structural changes in the lipid packing toward a more disordered conformation.

Fig. 5. Structural effects of RAs on DPPC monolayer studied by NR. A) Neutron reflectometry data including the best fits as a function of the scattering vector (RQ^4) for d_{62}DPPC monolayers with (dotted lines) and without (continuous lines) RAs at the air water (D_2O) interface at π=30 mN. The profiles are shifted along the y-axis for clarity. B) Scattering length density profiles for the best fits to the neutron reflection data.

To determine the structure and composition of the DPPC/RA monolayers, we used NR on Langmuir films at the air/water interface with four different isotropic contrasts. The reflectometry

profiles for d_{62}DPPC/RA mixtures on D_2O changed significantly when RAs were present and, in particular, the minimum at 0.08 $Å^{-1}$ shifted to higher Q following the ranking in this order: Cl_2DAA > DAA > NA (Fig. 5A), indicating changes in the overall structure of the monolayer.

For the fitting procedure, a two-layer model was applied, dividing the phospholipid monolayer into a head group layer and the acyl chain. The SLD (Supporting Information Table 1) of either the head group layer, the acyl chain or both were adjusted during the fitting procedure assuming the presence of 10 mol % RA to gain information of their co-localization within the DPPC monolayer. Alternatively, the fitting procedure was carried out under the assumption that no RA is present (see details in the Supporting Information). The chi^2-values obtained from the Monte Carlo fitting method (Supporting Information Fig. S4) allow comparing the quality of the applied models. From these values, it is likely that both Cl_2DAA and DAA co-localize within the acyl chain of DPPC. NA, on the other hand, might co-localize within the head group layer although, in this case, a fit of similar quality was found assuming the absence of NA in the film. The SLD profiles from the best d_{62}DPPC/RA fits to the NR data in Fig. 5A are shown in Fig. 5B. All other isotropic contrasts are displayed in the Supporting Information Fig. S4. Table 1 lists the main parameters used for the best fits shown in Fig. 4B and Supporting Information Fig. S4. The structural parameters for pure DPPC are in agreement with previous studies at similar π [38][39]. Cl_2DAA reduced the solvent penetration in the head group from 15 ± 5 to 6 ± 4 % and decreased the length of the tail from 16.2 ± 0.2 to 14.7 ± 0.1 Å, indicating an increase of the lipid tail tilt (t) using the relationship $\cos(t) = \frac{L}{L_{CH}}$ with L as the measured acyl chain length and L_{CH} as the maximal tail length [40]. When DAA was added to DPPC, the head group hydration and thickness decreased slightly, though within the fit error. DAA had no effect on the acyl chain tilt, whereas it decreased slightly for NA (the tail length decreased to 15.6 ± 0.1 Å). The roughness at the head group - tail interface was only increased by Cl_2DAA, from 3.7 ± 0.2 to 6.0 ± 0.2 Å.

Deuteration effects are known to affect the phase transition in lipids and the dynamics of molecules. In particular, the main phase transition from L_α to L_β decreases by 4 °C per tail for phospholipids due to deuteration [41]. The NR experiments were performed well below this phase transition and therefore we expect a similar order within the lipid chains. A small deviation may exist in the exact conformation of tails and their dynamics, however it is reasonable to assume that these differences are minor. Indeed, similar thermotropic effects using DSC were observed for RA on hydrogenated

or deuterated DPPC (Supporting Information Fig. S6 and Fig. 6). Further comparison of hydrogenated versus deuterated lipids could be performed by molecular dynamic simulations, but that remains out of the scope of the present work.

Table 1. Parameters used for the best the NR fits using a two layer model on DPPC/RA monolayer at 30 mN/m: lipid tail layer thickness, head group layer thickness, roughness between the head and the tail region. The head solvent penetration of DPPC is calculated in percentage (%) at π = 30 mN/m as described in section 2.5 [42]. The errors were calculated using the Monte Carlo method embebbed in Motofit [43].

3.3 Reduced cooperativity of the DPPC phase transition after RA integration

DSC (Fig. 6) and PT ssNMR (Fig. 7-8) experiments were performed to investigate the influence of RAs on the phase behavior as well as the molecular conformation of DPPC (Fig. 6 - 9). For DSC, vesicles were first well equilibrated above the melting temperature of DPPC and then subjected to 2 heating/cooling cycles yielding similar thermograms after extrusion (Supporting Information Fig. S6). The similarity between the heating thermograms of both heating cycles suggests that the samples were at equilibrium and did not show de-mixing during or prior to the re-heating cycles. The total heat excess during the main phase transition or the calorimetric enthalpy (ΔH) was calculated upon integration under each phase transition peak (Table 2). Additionally, ΔH_{vH} and the cooperativity unit, CU are given in Table 2. ΔH_{vH} corresponds to a simple two state model, while ΔH includes all changes independently of the model. Therefore, it is possible to calculate CU using these two values to asses information about the cooperativity of the main phase transition from the solid crystalline phase to the fluid phase, which has been thoroughly discussed in the literature [23].

Fig 6. Representative phase transition profiles of vesicles composed of DPPC and DPPC/RA (9:1, mol%). The enthalpy (cal/mole/C) is plotted as a function of the temperature for pure DPPC (solid line), DPPC/DAA (dotted broken line), DPPC/NA (broken line) and DPPC/Cl_2DAA (dotted line).

The DPPC profile in Fig. 6 shows the characteristic pre-transition onset of ΔH ~490 cal/mol/°C at 31°C. This peak corresponds to the transition from the planar gel phase ($L_{\beta'}$) to the rippled gel phase ($P_{\beta'}$). At 41°C, DPPC underwent a phase transition from the $P_{\beta'}$ to the liquid crystalline phase with ΔH ~12 kcal/mol/°C. The melting temperature (T_m) is derived as the maximum of the main transition peak. The sharpness of the peak indicates a highly cooperative phase transition typical for DPPC (CU = 44). Vesicles containing RA showed both peak broadening and a dramatic decrease of the maximum of the main phase transition enthalpy. This suggests a loss in

cooperativity. Additionally, the pre-transition peak displaying the L_β - $P_{\beta'}$ transition did not occur in the presence of RAs. For 10 mol% Cl_2DAA, ΔH decreased from 12.2 to 5.8 kcal/mol/°C and increased for DAA and NA to 14.2 and 17.9 kcal/mol/°C. Moreover, for NA and DAA, there was a significant shift in T_m from 41°C to 38°C. Thus, all RAs led to a decrease in cooperativity of the main phase transition of DPPC as indicated by the increase in CU. Note that CU decreased for 5 mol% Cl_2DAA from 44 to 27, but increased to 52 for 10 mol%. Such increase in CU is an artefact produced from the decrease of the transition peak for DPPC/Cl_2DAA compared to pure DPPC. The peak does not seem to broaden due to the loss of width at the same time. As a consequence, the width-height ratio suggests a cooperative phase transition. However, the data irrevocably indicate a drastic perturbation of the lipid packing for this particular RA.

Table 2. ΔH, ΔH_{vH}, CU and T_m values for DPPC and DPPC/RA vesicles. ΔH and T_m were directly calculated from the heat excess measured by the DSC, whereas ΔH_{vH} and CU were calculated as stated in the methodological section.

PT ssNMR data was collected for DPPC and DPPC mixtures in the lamellar phase containing 10 mol % NA or DAA for a detailed analysis of the phase transition. Fully hydrated DPPC and binary mixtures were investigated well below the phase transition at 25 °C in the L_β phase, above the melting point at 50 °C in the fluid lamellar phase, and at intermediate temperatures. In this way, the dynamics of different segments in DPPC can be followed throughout the entire melting process. The ^{13}C MAS NMR spectra display the data from experiments including the DP, INEPT and CP signals (Fig. 7).

For the L_α phase, the excellent resolution of the ^{13}C chemical shifts affords separate observation of each of the carbons of the choline moiety of the head group (α, β and γ), the glycerol backbone (g_1, g_2, and g_3), as well as several carbons of the acyl chains (1, 2, 3, 14, 15, and 16). The central segments of the acyl chains (4-13) give rise to a cluster of overlapping resonances at 30-32 ppm. The peak maximum at 31 ppm is indicative of a distribution of *trans* and gauche conformations typical of liquid hydrocarbons [36]. The signal amplitudes obtained with CP and INEPT can be rationalized in terms of the correlation time t_c and order parameter S_{CH} quantifying the rate and anisotropy of CH bond reorientation [33]. Intense INEPT and vanishing CP indicates fast isotropic reorientation (approximately $t_c < 10$ ns and $|S_{CH}| < 0.01$) characteristic of liquids with low viscosity.

Conversely, strong CP without INEPT can be observed for solids (t_c > 0.1 ms). Anisotropic liquids (t_c < 10 ns and 0.05 < $|S_{CH}|$ < 0.2) give rise to INEPT and CP signals with similar amplitudes.

The 45 °C data for all samples are characteristic of L_α phases with INEPT signals indicating fast reorientation of all segments (t_c < 10 ns). The absence of CP for the carbons of the CH_3 groups 16 and g show that these segments undergo isotropic reorientation. The comparable CP and INEPT amplitudes for most carbons verify that the phase is anisotropic.

At 25 °C, CP signals dominate for all samples consistent with the expected solid phases. Notable exceptions are the INEPT signals for the carbons g, and to some extent α and β, indicating that the choline moiety remains mobile even below the solid-to-liquid phase transition. The 33 ppm shift of the peak from the central segments of the acyl chains is a signature of an all-*trans* conformation. Taken together, these observations are consistent with an L_β phase with all-*trans* acyl chains and hydrated head groups.

According to the DSC data, the pure DPPC sample transforms from L_β to $P_{\beta'}$ at 33 °C. In the NMR data, this transition is mainly observed as a minor increase in the linewidth of the 33 ppm peak consistent with subtle differences in acyl chain packing for the troughs and ridges of the $P_{\beta'}$ phase. The transition from $P_{\beta'}$ to L_α gives rise to the appearance of INEPT signals for all carbons. The two-phase data at 37 °C is a superimposition of the one-phase $P_{\beta'}$ and L_α data at 35 and 39 °C, respectively. In particular, the peaks at 33 and 31 ppm show the coexistence of acyl chains in two distinct states: solid-like all-*trans* conformation and a liquid-like distribution of *trans*- and gauche conformations. For both RA samples, the transition from L_β to L_α is more continuous and lacks a clear two-phase region (Fig. 7 at 37 °C). Rather than having two pronounced maxima for the main acyl chain peak, there is a smooth transition between the shifts characteristic for the low and high temperature states.

Both, DSC and ssNMR data suggest that DPPC undergoes a phase transition at lower temperatures in the presence of DAA and NA. Data in Fig. 7 for DPPC and the DPPC/RA mixtures at 35 °C degrees displays the differences in the flexibility of the acyl chains at this temperature. Supporting Information Fig. S8 shows the expanded area from 20 – 40 ppm corresponding to $C_{2\text{-}15}$. The spectra for DPPC show no INEPT signal for any chain segment indicating that DPPC exists in its solid phase. Moreover, the peak at 32.8 ppm as well as the broadness of the CP signal for these peaks indicate an all-*trans* conformation for $C_{4\text{-}13}$ and thus support the gel phase for DPPC [44]. For DAA and NA, the spectra clearly showed INEPT signals and rather distinct peaks. The chemical shifts for

$C_{2\text{-}15}$ appear at 31.4 ppm and 31.6 ppm for DAA and NA, respectively, suggesting an ongoing phase transition. Overall, the data confirm a lower phase transition of DPPC/RA mixtures regardless of RA type, thus agreeing with the DSC data (Fig. 6). For future experiments it would be interesting to study detailed effects on the flexibility of certain segments in DPPC caused by Cl_2DAA for comparison.

Fig, 7. ^{13}C MAS NMR spectra (DP: gray; CP: blue; INEPT: red) of DPPC (A) and DPPC with 10 mol% DAA (B) and NA (C) from 25 to 50°C in the lamellar phase. Insets: Magnification of the spectral region of the lipid tails. The spectra were obtained with 125 MHz ^{13}C frequency, 5 kHz MAS and 48 kHz TPPM decoupling.

On the other hand, we observed different conformations of DPPC segments upon NA integration in the gel phase at 25 °C. The ^{13}C MAS NMR spectrum showed the appearance of a sharp CP peak at 14.13 ppm for the C_{16} methyl terminus at trans conformation in DPPC (Fig. 8A), whereas this peak broadened for DAA (Fig. 8B) and split in the presence of NA (Fig. 8C). Moreover, differences were observed for the C_α located in the head group at 59.3 ppm for NA only. This peak appeared as a sharp INEPT signal at 59.3 ppm, indicating fast ($\tau_c < 10$ ns) reorientation of the DPPC head groups (Fig.8).

Fig. 8. ^{13}C MAS NMR spectra (DP: gray; CP: blue; INEPT: red) of DPPC (A) and DPPC with 10 mol % DAA (B) and NA (C) at 25 °C. The spectra were obtained with 125 MHz ^{13}C frequency, 5 kHz MAS and 48 kHz TPPM decoupling. * Peaks corresponding to TRIS, which is used in the buffer.

4. Discussion

In this study, we performed DLS, PT ssNMR, NR, DSC, Cryo-TEM experiments on DPPC vesicles, monolayer and lamellar phase as well as DLS experiments on vesicles composed of the biologically relevant polar soybean lipid extract to unravel structural effects of three closely related RAs on a phospholipid bilayer. Furthermore, we determine the co-localization and of these RAs within DPPC monolayer and correlate changes on DPPC to the RAs toxicity.

DLS enabled us to obtain qualitatively comparable data for both model systems. Our DLS results (Fig. 2) suggest that RAs induce similar structural alterations on the size distribution of lipid vesicles for DPPC and the polar soy lipid extract. We found that DPPC/RA mixtures in the gel phase showed the formation of larger structures after 24 hours. In contrast, the liquid crystalline soy lipid/RA mixtures showed immediate effects on the vesicle sizes and signs of further vesicle growth

and accumulation after 24 hours. Therefore, the two lipid model systems are compared at two different time points to show similar extents of mixing as the dynamics of the system are expected to be different for fluid and gel membranes. By comparing the two model systems it can be concluded that Cl_2DAA and DAA induce major structural changes within phospholipid vesicles leading to significantly larger vesicle sizes, whereas the effect of NA led to a small increase in vesicle size distribution.

The DLS data was confirmed by Cryo-TEM that allowed visualizing elongated vesicles with lengths up to 250 nm for DPPC/RA mixtures for Cl_2DAA and DAA but not for NA (Fig. 3). NA led to slightly larger faceted vesicles suggesting minor effects on the structure of lipid vesicles. The tubular vesicles were mainly found in clusters, especially for Cl_2DAA. The clusters could be produced during the immobilization of the vesicles on the carbon grid due to the water removal. Besides mechanical causes, vesicle clustering occurs e.g. due to a decreased ability for hydrogen bond networking between the head groups and the bulk water as well as changes in the longer range hydration forces. Lower ability to hydrogen bonding is known to reduce the interlamellar space between bilayers and to increase intervesicular attraction as reported earlier using Raman scattering microscopy on 1- palmitoyl-2-oleoyl-sn-glycero-3-phosphocholine (POPC) bilayer [45]. The formation of microtubules suggests a significant change in the lipid packing. Previously, this type of membrane shape transformation was discussed in connection to peptides interacting with lipid bilayers [46]. Briefly, both the total interfacial area and acyl chain volume can be kept constant upon stretching a bilayer tubule as long as the diameter of the tubule decreases proportionally to the increase in vesicle length. However, the further bending of the lipid bilayer to form highly curved vesicles imposes a strain on a symmetric bilayer as the inner monolayer has a negative curvature, while the outer has a positive curvature. By changing the number or type of molecules in the inner relative to the outer monolayer of the vesicle bilayer, the relative area of the two monolayers will change although the total area in the bilayer remains constant. This could be achieved, for instance, by in plane phase separation within the vesicle membrane as observed for cardiolipin rich domains on the poles of *E.coli* [47]. Tubular structures were also observed earlier for milk fat globule membranes, composed by lipids with different packing parameters using Cryo-TEM [48]. However, the formation of highly curved areas does not directly correlate alone to phase separation within a phospholipid bilayer.

Despite the appearance of tubules, the structure of most vesicles in all DPPC/RA mixtures remained unaffected. This suggests that RAs distribute heterogeneously at the single vesicle level. This

heterogeneity is further supported by the PT ssNMR data showing a split of the peak for the acyl terminal methyl group for DPPC in the lamellar gel phase when NA was added (Fig. 8). Thus, DPPC exists in two distinguishable conformations upon the integration of NA at 25 °C in the gel phase. However, for spherical/faceted vesicles the presence of RAs cannot be excluded, yet, the RA concentration within these vesicles could be too low to alter the vesicle shape. Earlier studies have shown that compositional heterogeneity at the single vesicle level exists for binary lipid mixtures using atomic force microscopy [49] and fluorescence microscopy by the inclusion of two lipid fluorophores [50].

To further investigate packing effects of RAs on DPPC, Langmuir isotherm experiments were performed on the lipid monolayer. Our Langmuir data indeed confirmed changes in lipid packing upon RA insertion in the DPPC monolayer towards reduced compressibility in the LC-phase and a shift toward smaller MMA for all RAs (Fig. 4). The shift toward smaller MMA could be due to partial loss of lipid/RA molecules into the aqueous subphase and is therefore not further discussed. Partial material loss may also influence the reduction in compressibility. However, all RAs reduced the LE-LC coexisting region displayed by the shortened plateau at π = 15 mN/m in the isotherm (Fig. 4A) and shifted the minima in the compressibility moduli to higher π (Fig. 4B). This suggests a delay in the formation of the LC phase due to RA integration. To gain certainty about this effect, Brewster angle microscopy may visualize this expanding effect on DPPC monolayer in future experiments, as done in the past on pulmonary surfactants protein on lipid monolayer [51]. We note that the LC – LE plateau did not entirely disappear, which may facilitate a non-homogeneous distribution of RAs in the DPPC monolayer. Such a non-homogeneous effect could correlate well with the heterogeneous structural consequences at the bilayer level observed via Cryo-TEM and PT ssNMR (Fig. 3, 7-8). Although it has to be noted that the comparison between bilayer and monolayer systems does not necessarily yield similar effects due to the constraints imposed by the air-water interface.

In a recent study, a DPPC monolayer mixed with the monoterpenoid thymol were studied under similar conditions to the ones used in this work [52]. The authors observed similar changes in the π-A isotherms as the ones we report here in terms of compressibility modulus and concluded that the terpenes clearly had a fluidizing effect on DPPC monolayers. Our DSC and PT ssNMR data

570 confirmed the changes in membrane fluidity of DPPC bilayer in the presence of RAs (Fig. 6 and 7).
571 DAA and NA caused the earlier onset and broadening of the L_β-L_α phase transition of DPPC. The
572 earlier onset of the phase transition was visible at 35 °C in the 13C MAS NMR spectra due to the
573 INEPT signal, the shift from 32.8 to 31.4 ppm and a clear distinction of the peaks. Similar effects
574 were recently observed when linear monoterpenes were analyzed in DMPC membranes using PT
575 ssNMR [35]. Furthermore, the DSC results reveal a drastic loss of cooperativity (CU decrease) of
576 the phase transition that follows the trend Cl_2DAA > DAA > NA (Table 2). The integration of RAs
577 into DPPC bilayers could destabilize the DPPC crystalline phase in such a way that the forces in the
578 lattice are lowered to an extent that prevents a cooperative phase transition. Such an effect may be
579 accompanied with an increased mobility of the acyl chains and is supported by the small decrease in
580 T_m. This suggests a major disturbance of the lipid packing consistent with an increased disorder of
581 lipid configurations (Table 2). The increased molecular disorder is supported by: 1) the decreased
582 compression modulus observed in our monolayer studies (Fig. 4) and 2) coexisting DPPC
583 configurations in our PT ssNMR data (Fig. 8) for DPPC bilayer. Similar impact on the thermotropic
584 behavior of lipids as studied by DSC, were reported for abietic acid/DPPC [7] and rosmarinic
585 acid/DMPC systems (their chemical structure is related to the ones used in this study) [6]. Such
586 perturbing effect on the thermotropic behavior of lipid membranes for RAs was previously linked to
587 their toxicity [53]. Our data also suggests that besides the correlation between the toxicity of RAs
588 and the thermotropic effect on the main phase transition of DPPC, there is a correlation with the
589 presence of coexisting lipid configurations at 25 °C for NA and the ability to induce highly curved
590 elongated vesicular structures for DAA and Cl_2DAA.

591

592 For structural details, NR measurements were taken out on Langmuir films to study the molecular
593 geometry of DPPC/RA monolayer at the air-water interface. The best fit for DPPC monolayers
594 containing Cl_2DAA and DAA was achieved when these particular RAs where co-localized in the
595 acyl chain region (Supporting Information Fig. S4). The overall geometry of DPPC changed upon
596 Cl_2DAA integration in terms of a decreased acyl chain length thickness from 16.2 ± 0.2 to 14.4 ±
597 0.1 Å and increased roughness from 3.7 ± 0.2 Å to 6.0 ± 0.2 Å at the head to tail interfacial region
598 (Table 1). These effects confirmed changes in the lipid packing toward a more disordered lipid
599 packing, and the integration of this particular RA into the lipid tail region. DAA, which differs from
600 Cl_2DAA only in the absence of the two chlorine atoms, seemed also to co-localize within the acyl
601 chain, yet there were no effects on the acyl chain length or any further interfacial roughening. These

differences may be caused by the presence of the two bulky chlorine atoms in Cl_2DAA leading to a drastic perturbation in the acyl chain packing due to their large van der Waals radii and steric effects they may induce. The main effect caused by DAA on DPPC was the shortening of the head group region. In contrast, NA is likely to integrate into the head group region of DPPC as determined by NR (Supporting Information Fig. S4). A fit to the NR data of similar quality could be found assuming that NA was absent from the Langmuir monolayer. This could be due to lower contrast between the NA and DPPC head groups or that the actual NA concentration in the Langmuir film was lower than the nominal composition due to NA molecules being expelled into the aqueous phase. However, the effects in Langmuir film compressibility, PT ssNMR signals, and the low aqueous solubility of 2.31 mg/L suggest that NA is indeed kept in the lipid layer [54]. The best fits to the NR data showed minimal effects on the head group and a slight decrease in the acyl chain thickness from 16.2 ± 0.2 to 15.6 ± 0.1 Å. This was accompanied by a slight increase in solvent penetration into the head group region from 15 ± 5 to 21 ± 5 %, although within the fit error (Table 1). Our PT ssNMR results indeed support increased mobility of the DPPC head group region as displayed by the INEPT peak for the C_α carbon (Fig. 9). This INEPT signal in the ^{13}C MAS spectra shows all head groups in a mobile conformation at this particular position, which may be caused by the integration of NA. Furthermore, NA affected the acyl chain, since the CP signal at 14.3 ppm split indicating the terminus methyl group in the acyl chain to exist in two different conformations or environments (Fig. 8): either as two distinct solid phases, as a single phase with two distinct locations of the DPPC molecules, or as a single phase where all DPPC molecules are equivalent but with different conformations of the sn1- and sn2- termini. Thus, it is likely that NA co-localizes in the head group region of DPPC.

In summary, the formation of tubular vesicular structures correlates with the suggested co-localization of RAs in the acyl chain region of DPPC and increased conformational disorder in the lipid bilayer. The data suggests that RAs may induce a change in the packing parameter. The critical packing parameter (P) is calculated by

$$P = \frac{V}{S_o\, l_c}$$

where V is the molecular volume, S_o is the surface cross section of the head group and l_c is the length of the acyl chain [55]. For NA, where no incorporation on the lipid tail occurs, increased

mobility in the head group suggests an increased head group area that seems to be compensated by the tilting of the DPPC chain to maintain a packing parameter close to 1 and therefore the spherical, facetted vesicle structure prevailed. For DAA and Cl_2DAA, on the other hand, the incorporation into the acyl tail is more likely to induce a shift of the packing parameter towards smaller values and the possibility to accommodate for the highly curved poles of the tubular vesicles. Similar space filling models have been proposed earlier that show the changes in lipid packing to optimize the van der Waals forces between lipids and structural consequences for the lipid shape [56]. More recently, fluorescence microscopy was used to show that cardiolipin, a cone inverted lipid present in *E coli*, enriches the regions of *E.coli* with high curvature such as poles and septa [47]. Note that Langmuir isotherms and NR experiments are performed at the air-water interface, and therefore the studies are made on lipid monolayers. This may impose an additional constraint against the induction of high curvature structures due to changes in P. This is in contrast to the other techniques in this work performed on lipid vesicles, which can respond to changes in P. Schematics of our proposed model for RA incorporation into the membrane and its effect on the overall structure of lipid bilayers are shown in Fig. 9.

Fig. 9. Proposed impact of the integration of different RAs, NA (blue) and DAA (yellow), on the structure of the DPPC bilayer and the consequences for the macrostructure of unilamellar vesicles. DAA co-localizes within the lipid tail region, whereas NA co-localizes at the head-tail interface both affecting the lipid packing to different extents. The higher polarity and/or increased rigidness of DAA (and bulkiness of Cl_2DAA) may be responsible for changes in the lipid packing affecting the curvature at the vesicle level and this, in turn, can be correlated with the increased toxicity of these particular RAs.

5. Conclusion

RAs integrate into phospholipid membranes and induce significant effects on the thermotropic and structural properties of lipid bilayers. The extent in which the DPPC packing parameter is affected follows the trend Cl_2DAA > DAA > NA. This trend follows the polarity of these RAs, which can be displayed by their dipole moment: Cl_2DAA (3.1 D) > DAA (1.9 D) > NA (1.7 D) [57]. Moreover, this trend follows each RA's molecular mobility. Briefly, the chemical difference between Cl_2DAA and DAA are two synthetically added bulky chlorine atoms at C_{14} and C_{12}. Due to the relatively large van der Waals radius of chlorine, the chlorine atoms may cause steric fixation and loss of flexibility within the molecule, especially on the isopropane group. Both, Cl_2DAA and DAA share an aromatic ring with a planar ring geometry in contrast to NA [58]. Moreover, the presence of the aromatic ring (π-π stacking) and chlorine groups increase the polarizability of Cl_2DAA and DAA as

compared to NA. The extent of these effects can be correlated to the toxicity of RAs. More specifically, we have shown that the more toxic DAA and Cl_2DAA co-localize in the lipid tail region and therefore induce mainly changes in this region that lead to alterations in the membrane fluidity, curvature and shape. Particularly, Cl_2DAA with two relatively large chlorine atoms perturbs the interface between the head group and tail region of lipid monolayers due to roughening of the membrane and a reduction of the head group hydration showing the strongest effects on phospholipid bilayer structure. This promotes the stretching of the phospholipid membrane and the formation of tubular vesicular structures. In contrast, the least toxic NA, has its main effects on the head group region enabling the compensation of perturbing effects by the acyl chain tilt. NA is the least polarizable and most flexible of the RA studied, and it can be incorporated in the membrane, to a larger extent, without compromising the functionality of the lipid membrane.

Graphical abstract

Same as Figure 9.

Acknowledgement:

The authors wish to thank the Institute Laue Langevin (France) and ISIS at the Rutherford Appleton Laboratory (UK) for allocated beam times and in particular Max Skoda (ISIS) for excellent local support. We thank Dr. Gunnel Karlsson for great technical support during CRYO-TEM imaging, Prof. Kell Mortensen for access to DSC (University of Copenhagen) and Göran Carlström for technical support during NMR (Lund University). We acknowledge funding from the Swedish Research Council, DANSCATT Centre (Danish government), the Research Centre 'bioSYNergy' funded by the UCPH Excellence programme for interdisciplinary Research and the Innovation Fund Denmark via the project "Plant Power: Light driven synthesis of complex terpenoids using cytochrome P450s".

References

[1] C.I. Keeling, J. Bohlmann, Diterpene resin acids in conifers., Phytochemistry. 67 (2006) 2415–23. doi:10.1016/j.phytochem.2006.08.019.

[2] S. Savluchinske Feio, B. Gigante, J. Carlos Roseiro, M.J. Marcelo-Curto, Antimicrobial activity of diterpene resin acid derivatives, J. Microbiol. Methods. 35 (1999) 201–206. doi:10.1016/S0167-7012(98)00117-1.

[3] H.R.Lerner, Plant Responses to Environmental Stresses: From Phytohormones to Genome Reorganization, 1999.

[4] A.K. Choudhary, S. Kumar, C. Sharma, Removal of Chlorophenolics From Pulp and Paper Mill Wastewater Through Constructed Wetland, Water Environ. Res. 85 (2013) 54–62. doi:10.2307/42569408.

[5] S. a. Mendanha, S.S. Moura, J.L. V Anjos, M.C. Valadares, A. Alonso, Toxicity of terpenes on fibroblast cells compared to their hemolytic potential and increase in erythrocyte membrane fluidity, Toxicol. Vitr. 27 (2012) 323–329. doi:10.1016/j.tiv.2012.08.022.

[6] L. Pérez-Fons, F.J. Aranda, J. Guillén, J. Villalaín, V. Micol, Rosemary (Rosmarinus officinalis) diterpenes affect lipid polymorphism and fluidity in phospholipid membranes, Arch. Biochem. Biophys. 453 (2006) 224–236. doi:10.1016/j.abb.2006.07.004.

[7] F.J. Aranda, J. Villalaín, The interaction of abietic acid with phospholipid membranes., Biochim. Biophys. Acta. 1327 (1997) 171–80. http://www.ncbi.nlm.nih.gov/pubmed/9271259.

[8] S. Ali, S. Minchey, a Janoff, E. Mayhew, A differential scanning calorimetry study of phosphocholines mixed with paclitaxel and its bromoacylated taxanes., Biophys. J. 78 (2000) 246–256. doi:10.1016/S0006-3495(00)76588-X.

[9] T.A. Söderberg, R. Gref, S. Holm, T. Elmros, G. Hallmans, Antibacterial Activity of Rosin and Resin Acids in Vitro, Scand. J. Plast. Reconstr. Surg. Hand Surg. 24 (1990) 199–205. doi:10.3109/02844319009041279.

[10] N. Cherr, M. Shenker, Toxic effects of selected bleached kraft mill effluent consituents on the sea urichin sperm cell, 6 (1987) 561–569.

[11] index @ www.avantilipids.com, (n.d.). https://www.avantilipids.com/index.php?option=com_content&view=article&id=415&Itemid=124&catnumber=541602.

[12] K. Jacobson, D. Papahadjopoulos, Phase transitions and phase separations in phospholipid membranes induced by changes in temperature, pH, and concentration of bivalent cations., Biochemistry. 14 (1975) 152–161. doi:10.1021/bi00672a026.

[13] A.P. Lipids, Avanti Polar Lipids Inc., Material Safety Data Sheet, (2015). http://avantilipids.com/MSDS/msds.php?ProdNum=880126P&format=raw.

[14] D.J. McClements, E. Vittadini, Y. Vodovotz, Understanding and Controlling the Microstructure of Complex Foods, Underst. Control. Microstruct. Complex Foods. (2007) 89–112. doi:10.1533/9781845693671.1.89.

[15] F. Kreith, CRC Handbook of Thermal Engineering, CRC Press, 2010. https://books.google.com/books?id=M0NgOBAYmCkC&pgis=1 (accessed March 13, 2015).

[16] Microscope/Lund, Philips C. BioTWIN Cryo. (2016). http://www.polymat.lth.se/nchrem/microscopes/ (accessed January 5, 2016).

[17] N.B. Vargaftik, B.N. Volkov, L.D. Voljak, International Tables of the Surface Tension of Water, J. Phys. Chem. Ref. Data. 12 (1983) 817. doi:10.1063/1.555688.

[18] R. a. Campbell, H.P. Wacklin, I. Sutton, R. Cubitt, G. Fragneto, FIGARO: The new horizontal neutron reflectometer at the ILL, Eur. Phys. J. Plus. 126 (2011) 107. doi:10.1140/epjp/i2011-11107-8.

[19] J.R.P. Webster, S. Langridge, R.M. Dalgliesh, T.R. Charlton, Reflectometry techniques on the second target station at ISIS: Methods and science, Eur. Phys. J. Plus. 126 (2011) 1–5. doi:10.1140/epjp/i2011-11112-y.

[20] W. Stillwell, An Introduction to Biological Membranes, Elsevier, 2013. doi:10.1016/B978-0-444-52153-8.00011-8.

[21] A. Nelson, Co-refinement of multiple-contrast neutron/X-ray reflectivity data using MOTOFIT, J. Appl. Crystallogr. 39 (2006) 273–276. doi:10.1107/S0021889806005073.

[22] J. Sturtevant, Biochemical Applications Of Differential Scanning Calorimetry, Annu. Rev. Phys. Chem. 38 (1987) 463–488. doi:10.1146/annurev.physchem.38.1.463.

[23] G. Bruylants, J. Wouters, C. Michaux, Differential scanning calorimetry in life science: thermodynamics, stability, molecular recognition and application in drug design., Curr. Med. Chem. 12 (2005) 2011–2020. doi:10.2174/0929867054546564.

[24] E.R. Andrew, A. Bradbury, R.G. Eades, Nuclear Magnetic Resonance Spectra from a Crystal rotated at High Speed, Nature. 182 (1958) 1659–1659. doi:10.1038/1821659a0.

[25] A.E. Bennett, C.M. Rienstra, M. Auger, K. V Lakshmi, R.G. Griffin, Heteronuclear decoupling in rotating solids, J. Chem. Phys. 103 (1995) 6951–6958. doi:10.1063/1.470372.

[26] R.K. Harris, E.D. Becker, S.M. De Cabral Menezes, P. Granger, R.E. Hoffman, K.W. Zilm, Further Conventions for NMR shielding and chemical shifts (IUPAC recommendations 2008), Magn. Reson. Chem. 46 (2008) 582–598. doi:10.1002/mrc.2225.

[27] A. Pines, M.G. Gibby, J.S. Waugh, Proton-enhanced nuclear induction spectroscopy 13C chemical shielding anisotropy in some organic solids, Chem. Phys. Lett. 15 (1972) 373–376. doi:10.1016/0009-2614(72)80191-X.

[28] G. a. Morris, R. Freeman, Enhancement of Nuclear Magnetic Resonance Signals by Polarization Transfer, J. Am. Chem. Soc. 233 (1979) 760–762. doi:Doi 10.1021/Ja00497a058.

[29] A.L. van Geet, Calibration of Methanol Nuclear Magnetic Resonance Thermometer at Low Temperature Simultaneous Spectrophotometric Determination of Hydrogen Peroxide and Peroxyacids of Sulfur, Anal. Chem. 42 (1970) 679–680. doi:10.1021/ac60288a022.

[30] L. Chen, Z. Weng, L. Goh, M. Garland, An efficient algorithm for automatic phase correction of NMR spectra based on entropy minimization, J. Magn. Reson. 158 (2002) 164–168. doi:10.1016/S1090-7807(02)00069-1.

[31] J.D. van Beek, matNMR: A flexible toolbox for processing, analyzing and visualizing magnetic resonance data in Matlab??, J. Magn. Reson. 187 (2007) 19–26. doi:10.1016/j.jmr.2007.03.017.

[32] A. Nowacka, P.C. Mohr, J. Norrman, R.W. Martin, D. Topgaard, Polarization transfer solid-state NMR for studying surfactant phase behavior, Langmuir. 26 (2010) 16848–16856. doi:10.1021/la102935t.

[33] A. Nowacka, N.A. Bongartz, O.H.S. Ollila, T. Nylander, D. Topgaard, Signal intensities in 1H-13C CP and INEPT MAS NMR of liquid crystals, J. Magn. Reson. 230 (2013) 165–175. doi:10.1016/j.jmr.2013.02.016.

[34] A. Nowacka, S. Douezan, L. Wadsö, D. Topgaard, E. Sparr, Small polar molecules like glycerol and urea can preserve the fluidity of lipid bilayers under dry conditions, Soft Matter. 8 (2012) 1482. doi:10.1039/c1sm06273e.

[35] Q.D. Pham, D. Topgaard, E. Sparr, Cyclic and Linear Monoterpenes in Phospholipid Membranes: Phase Behavior, Bilayer Structure, and Molecular Dynamics, Langmuir. 31 (2015) 11067–11077. doi:10.1021/acs.langmuir.5b00856.

[36] W.L. Earl, D.L. VanderHart, Observations in Solid Polyethylenes by Carbon-13 Nuclear Magnetic Resonance with Magic Angle Sample Spinning, Macromolecules. 12 (1979) 762–767. doi:10.1021/ma60070a045.

[37] J. Seelig, A. Seelig, Lipid conformation in model membranes and biological membranes., Q. Rev. Biophys. 13 (1980) 19–61. doi:10.1017/S0033583500000305.

[38] D. Vaknin, K. Kjaer, J. Als-Nielsen, M. Lösche, Structural properties of phosphatidylcholine in a monolayer at the air/water interface, Biophys. J. 59 (1991) 1325–1332. doi:10.1016/S0006-3495(91)82347-5.

[39] A.P. Dabkowska, L.E. Collins, D.J. Barlow, R. Barker, S.E. Mclain, M.J. Lawrence, et al., Modulation of dipalmitoylphosphatidylcholine monolayers by dimethyl sulfoxide, Langmuir. 30 (2014) 8803–8811. doi:10.1021/la501275h.

[40] R.M. Moebius, Novel Methods to Study Interfacial Layers, 1st Editio, Elsevier Science, 2001.

[41] M.K. and S.I.C. Nils O Petersen, Paulus A Kroon, Thermal phase transitions in deuterated lecithin bilayers, Chem. Physicss Lipids 14. 14 (1975) 343–349.

[42] J. Ulander, A.D.J. Haymet, Permeation across hydrated DPPC lipid bilayers: simulation of the titrable amphiphilic drug valproic acid., Biophys. J. 85 (2003) 3475–3484. doi:10.1016/S0006-3495(03)74768-7.

[43] A. Nelson, Co-refinement of multiple-contrast neutron/X-ray reflectivity data using MOTOFIT, J. Appl. Crystallogr. 39 (2006) 273–276. doi:10.1107/S0021889806005073.

[44] T. Mavromoustakos, E. Theodoropoulou, D.P. Yang, The use of high-resolution solid-state NMR spectroscopy and differential scanning calorimetry to study interactions of anaesthetic steroids with membrane, Bba.Biomembranes. 1328 (1997) 65–73.

[45] J.-X. Cheng, S. Pautot, D.A. Weitz, X.S. Xie, Ordering of water molecules between phospholipid bilayers visualized by coherent anti-Stokes Raman scattering microscopy., Proc. Natl. Acad. Sci. U. S. A. 100 (2003) 9826–9830. doi:10.1073/pnas.1732202100.

[46] Y. a Domanov, P.K.J. Kinnunen, Antimicrobial peptides temporins B and L induce formation of tubular lipid protrusions from supported phospholipid bilayers., Biophys. J. 91 (2006) 4427–4439. doi:10.1529/biophysj.106.091702.

[47] L.D. Renner, D.B. Weibel, Cardiolipin microdomains localize to negatively curved regions of Escherichia coli membranes., Proc. Natl. Acad. Sci. U. S. A. 108 (2011) 6264–6269. doi:10.1073/pnas.1015757108.

[48] R. Waninge, T. Nylander, M. Paulsson, B. Bergenståhl, Milk membrane lipid vesicle structures studied with Cryo-TEM, Colloids Surfaces B Biointerfaces. 31 (2003) 257–264. doi:10.1016/S0927-7765(03)00145-0.

[49] A. Åkesson, T. Lind, N. Ehrlich, D. Stamou, H. Wacklin, M. Cárdenas, Composition and structure of mixed phospholipid supported bilayers formed by POPC and DPPC, Soft Matter. 8 (2012) 5658. doi:10.1039/c2sm00013j.

[50] J. Larsen, N.S. Hatzakis, D. Stamou, Observation of inhomogeneity in the lipid composition of individual nanoscale liposomes, J. Am. Chem. Soc. 133 (2011) 10685–10687. doi:10.1021/ja203984j.

[51] A. Cruz, L. Vázquez, M. Vélez, J. Pérez-Gil, Effect of pulmonary surfactant protein SP-B on the micro- and nanostructure of phospholipid films., Biophys. J. 86 (2004) 308–320. doi:10.1016/S0006-3495(04)74106-5.

[52] J.V.N. Ferreira, T.M. Capello, L.J.A. Siqueira, J.H.G. Lago, L. Caseli, Mechanism of Action of Thymol on Cell Membranes Investigated through Lipid Langmuir Monolayers at the Air–Water Interface and Molecular Simulation, Langmuir. 32 (2016) 3234–3241. doi:10.1021/acs.langmuir.6b00600.

[53] H.S. Camargos, R.A. Moreira, S.A. Mendanha, K.S. Fernandes, M.L. Dorta, A. Alonso, Terpenes increase the lipid dynamics in the Leishmania plasma membrane at concentrations similar to their IC50 values, PLoS One. 9 (2014). doi:10.1371/journal.pone.0104429.

[54] G. Peng, J.C. Roberts, Solubility and toxicity of resin acids, Water Res. 34 (2000) 2779–2785. doi:10.1016/S0043-1354(99)00406-6.

[55] J.N. Israelachvili, D.J. Mitchell, B.W. Ninham, Theory of self-assembly of hydrocarbon amphiphiles into micelles and bilayers, J. Chem. Soc. Faraday Trans. 2. 72 (1976) 1525. doi:10.1039/f29767201525.

[56] T.J. McIntosh, Differences in hydrocarbon chain tilt between hydrated phosphatidylethanolamine and phosphatidylcholine bilayers. A molecular packing model, Biophys. J. 29 (1980) 237–245. doi:10.1016/S0006-3495(80)85128-9.

[57] C.L. Yaws, Yaws' Handbook of Thermodynamic and Physical Properties of Chemical Compounds, Knovel, 2003. http://app.knovel.com/web/toc.v/cid:kpYHTPPCC4/ (accessed December 10, 2015).

[58] T.M. Krygowski, Crystallographic studies of inter- and intramolecular interactions reflected in aromatic character of Pi-electron systems, J. Chem. Inf. Model. 33 (1993) 70–78. doi:10.1021/ci00011a011.

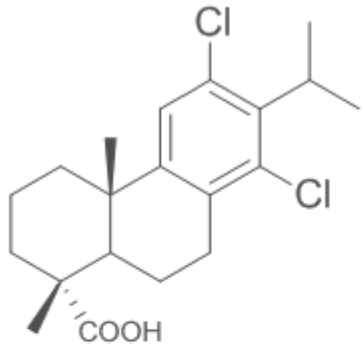

Dichlorodehydroabietic acid

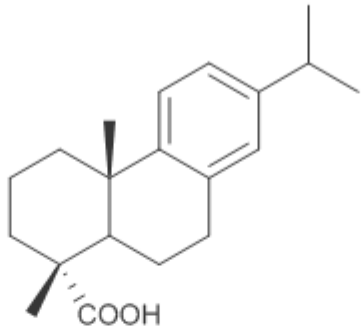

Dehydroabietic acid

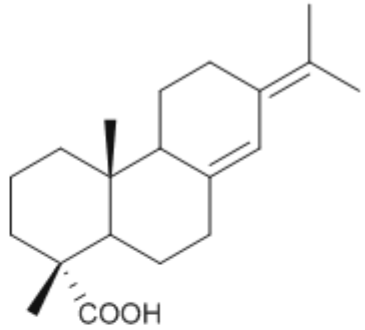

Neoabietic acid

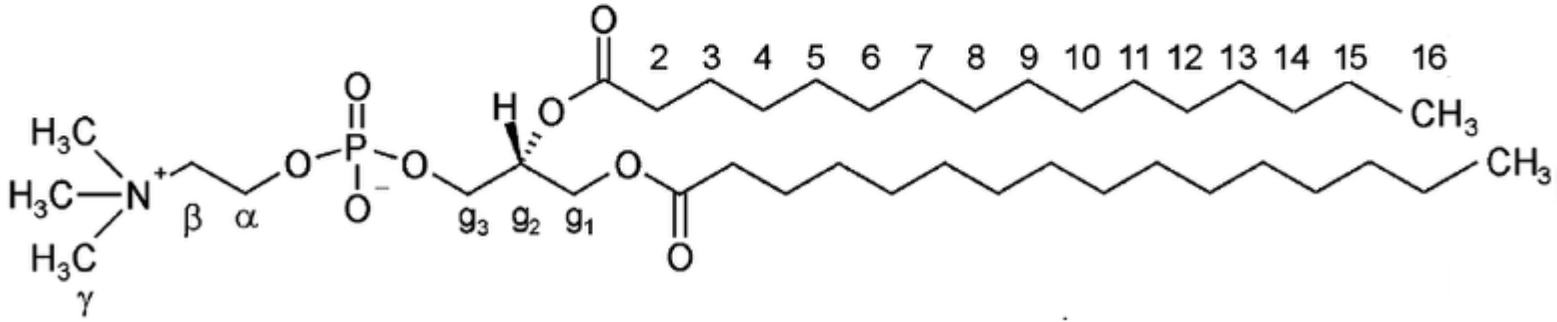

Dipalmitoylphosphatidylcholine

A

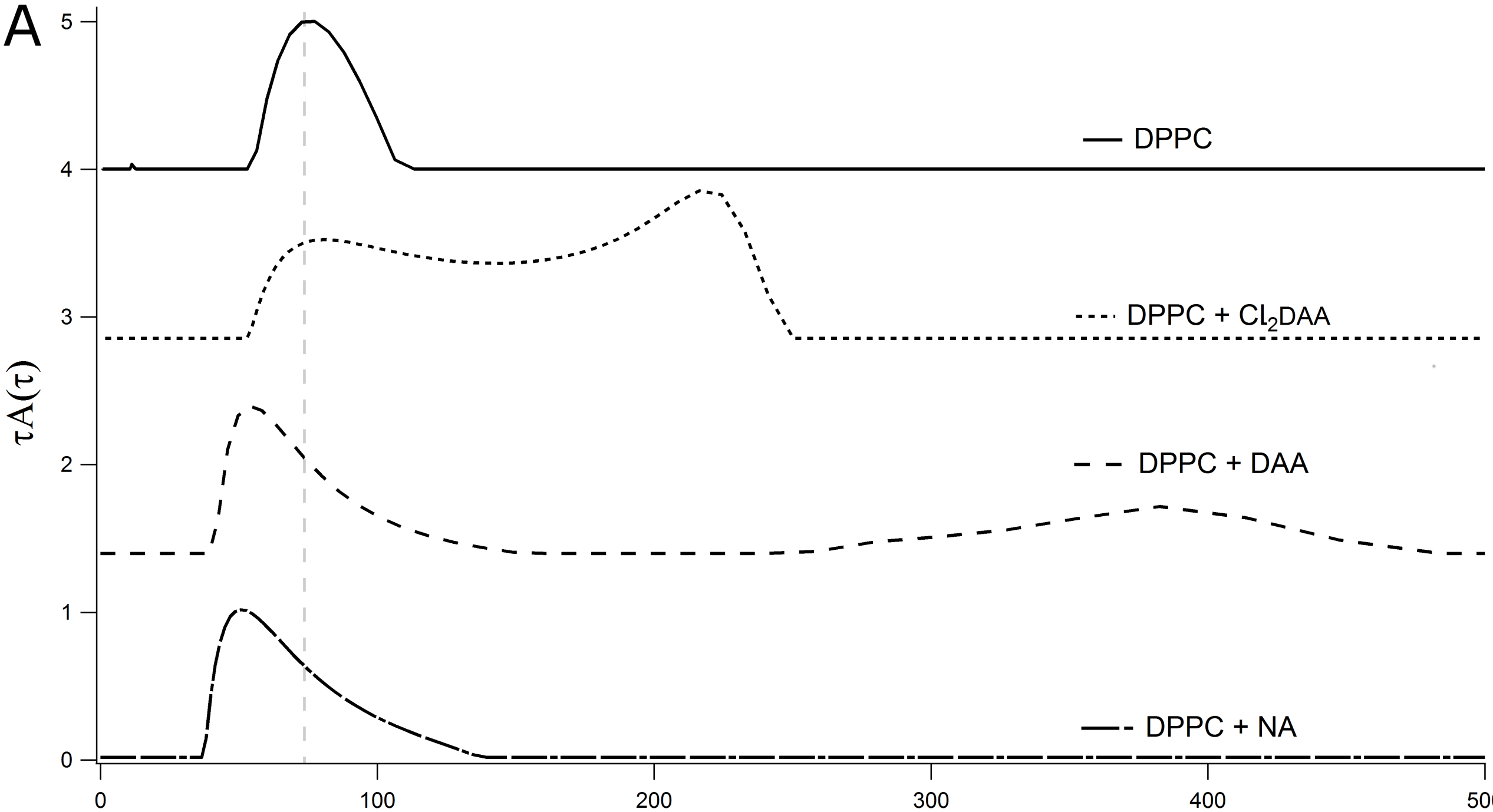
5
4
3
2
1
0
τA(τ)
DPPC
DPPC + Cl2DAA
DPPC + DAA
DPPC + NA
0
100
200
300
400
500
Size Radius (nm)

B

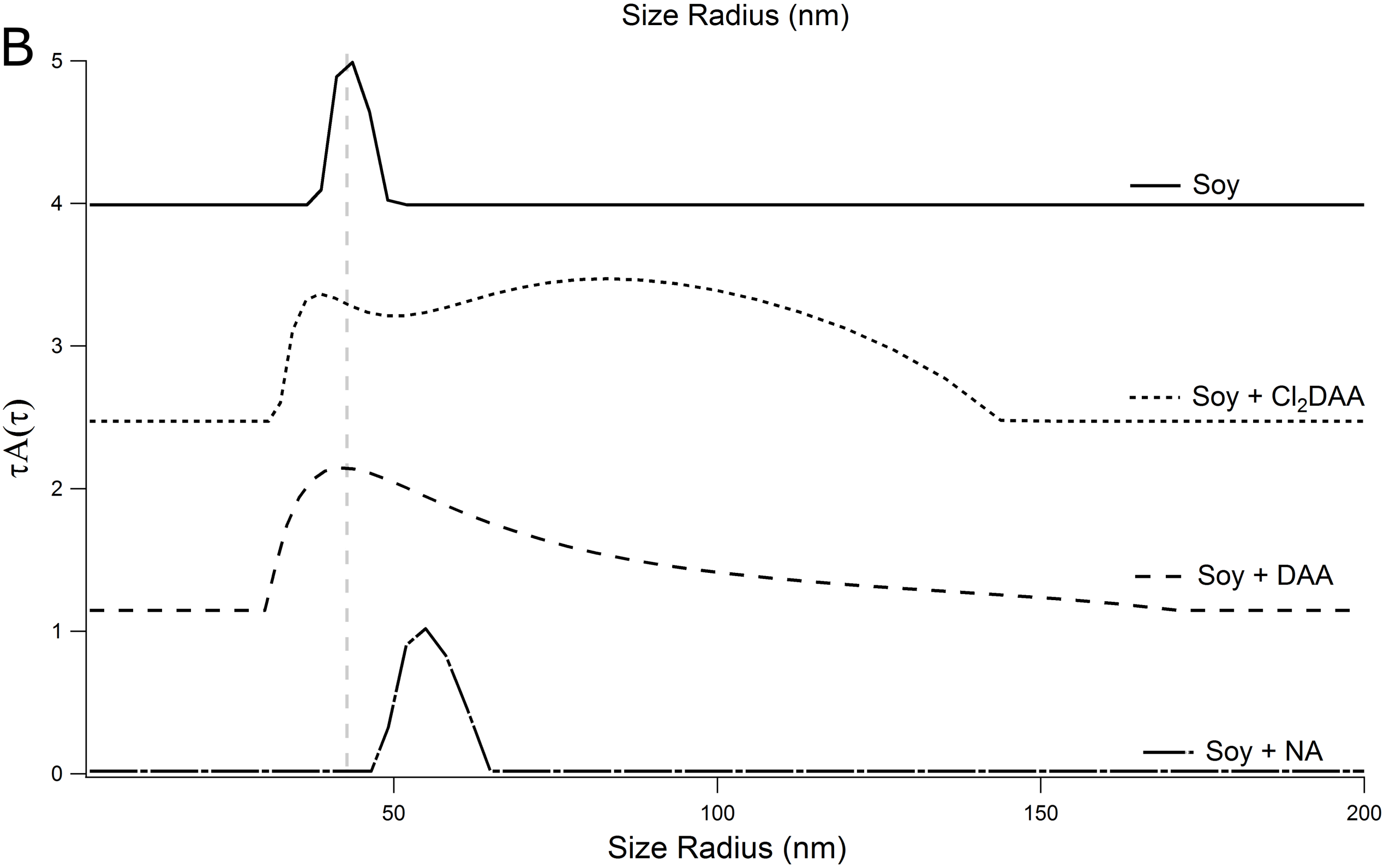
5
4
3
2
1
0
τA(τ)
Soy
Soy + Cl2DAA
Soy + DAA
Soy + NA
50
100
150
200
Size Radius (nm)

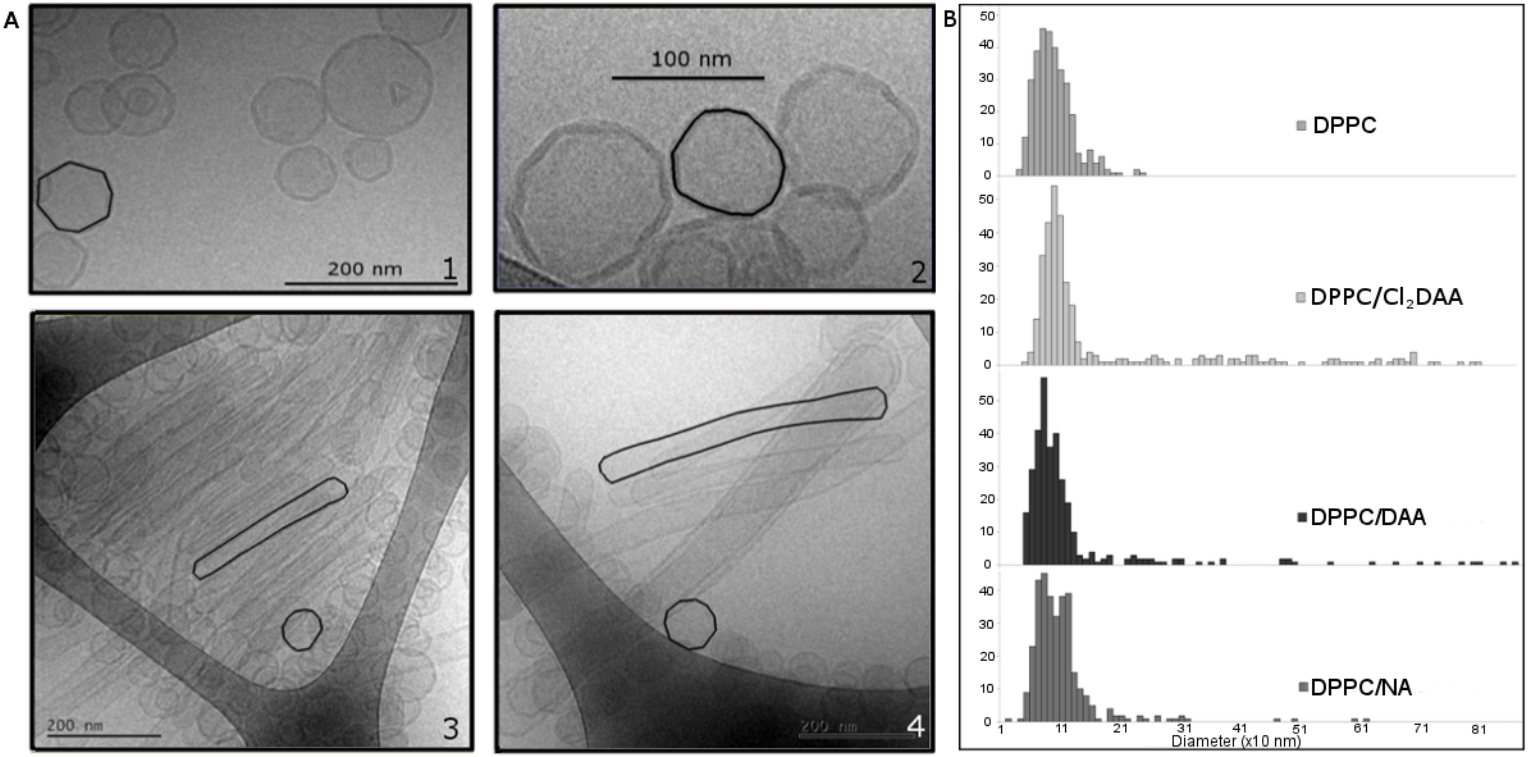
A
200 nm
1
100 nm
2
200 nm
3
200 nm
4
B
DPPC
DPPC/Cl2DAA
DPPC/DAA
DPPC/NA
Diameter (x10 nm)

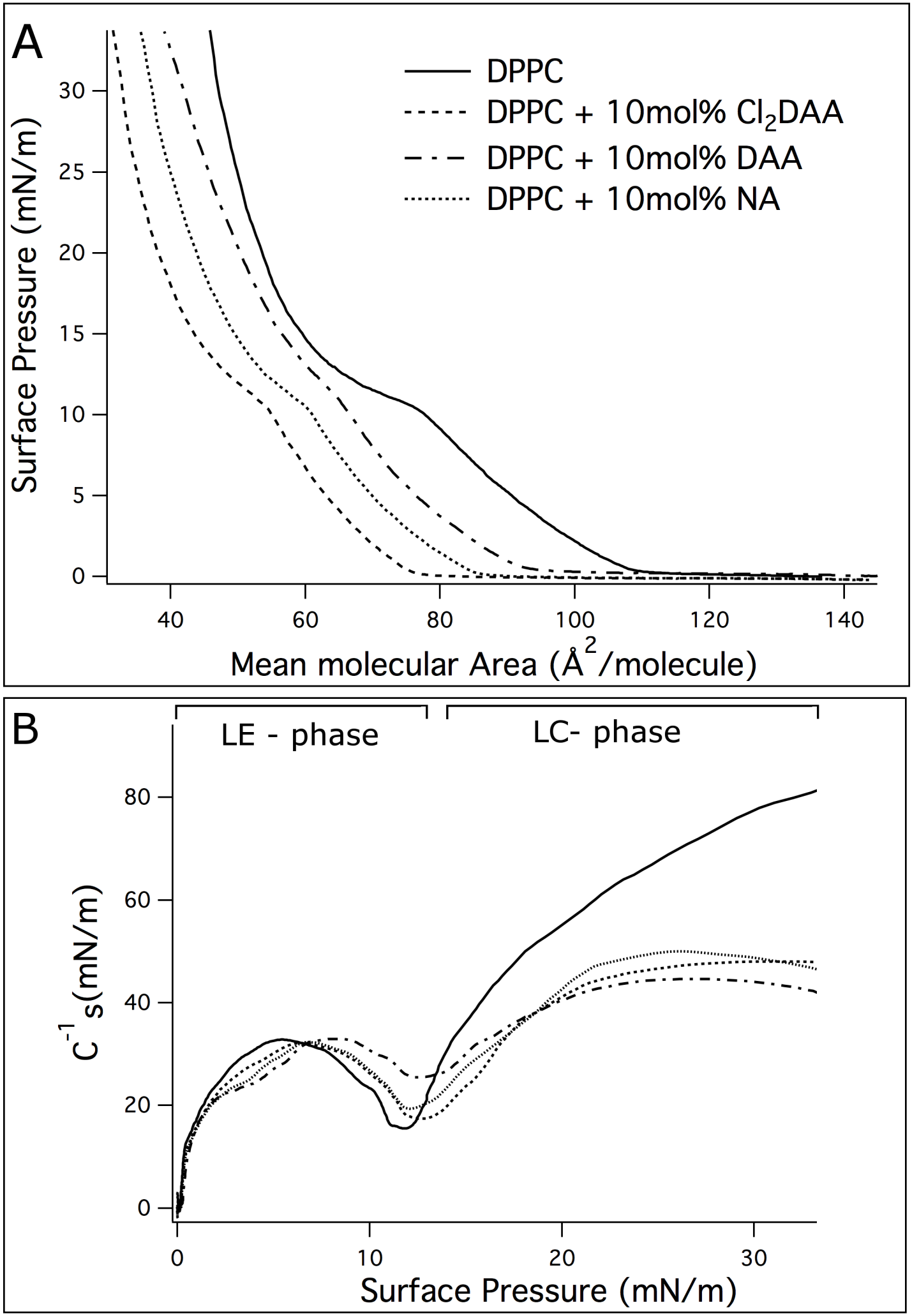
A
DPPC
DPPC + 10mol% Cl2DAA
DPPC + 10mol% DAA
DPPC + 10mol% NA
Surface Pressure (mN/m)
Mean molecular Area (Å2/molecule)
B
LE - phase
LC- phase
C-1 s(mN/m)
Surface Pressure (mN/m)

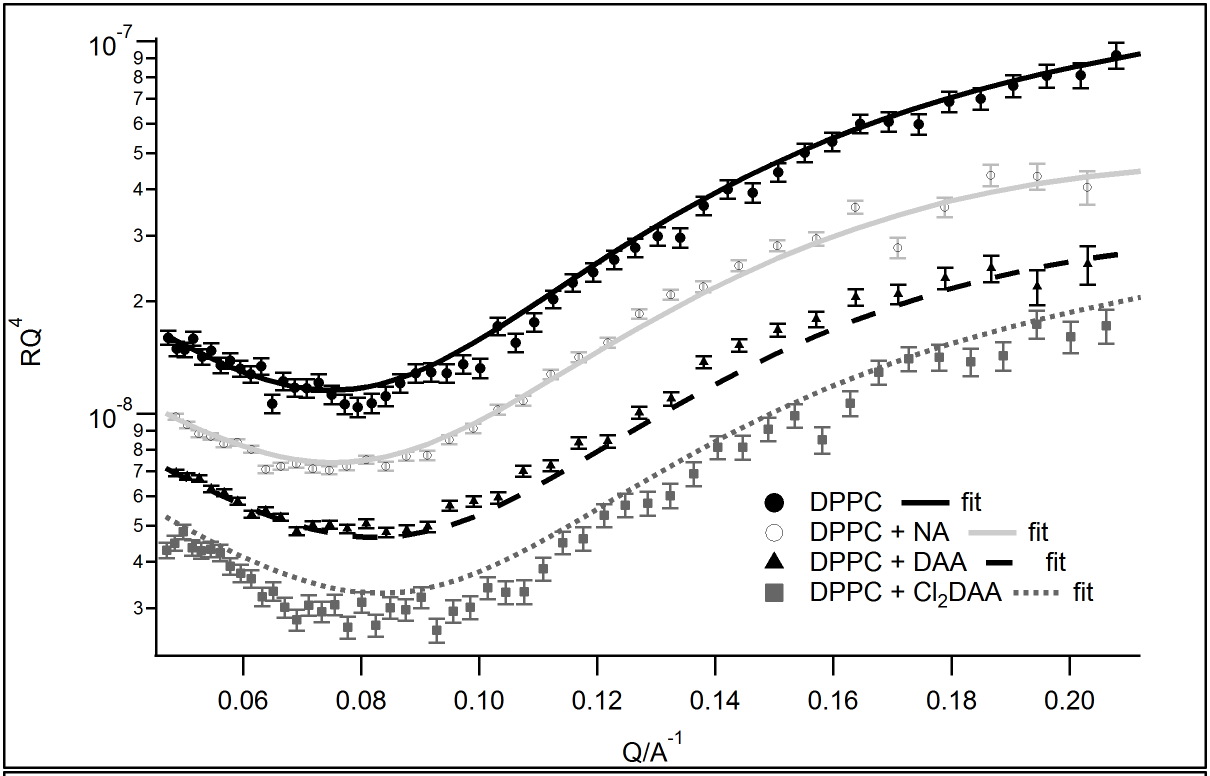
RQ^4
Q/A^-1
DPPC
fit
DPPC + NA
fit
DPPC + DAA
fit
DPPC + Cl2DAA
fit

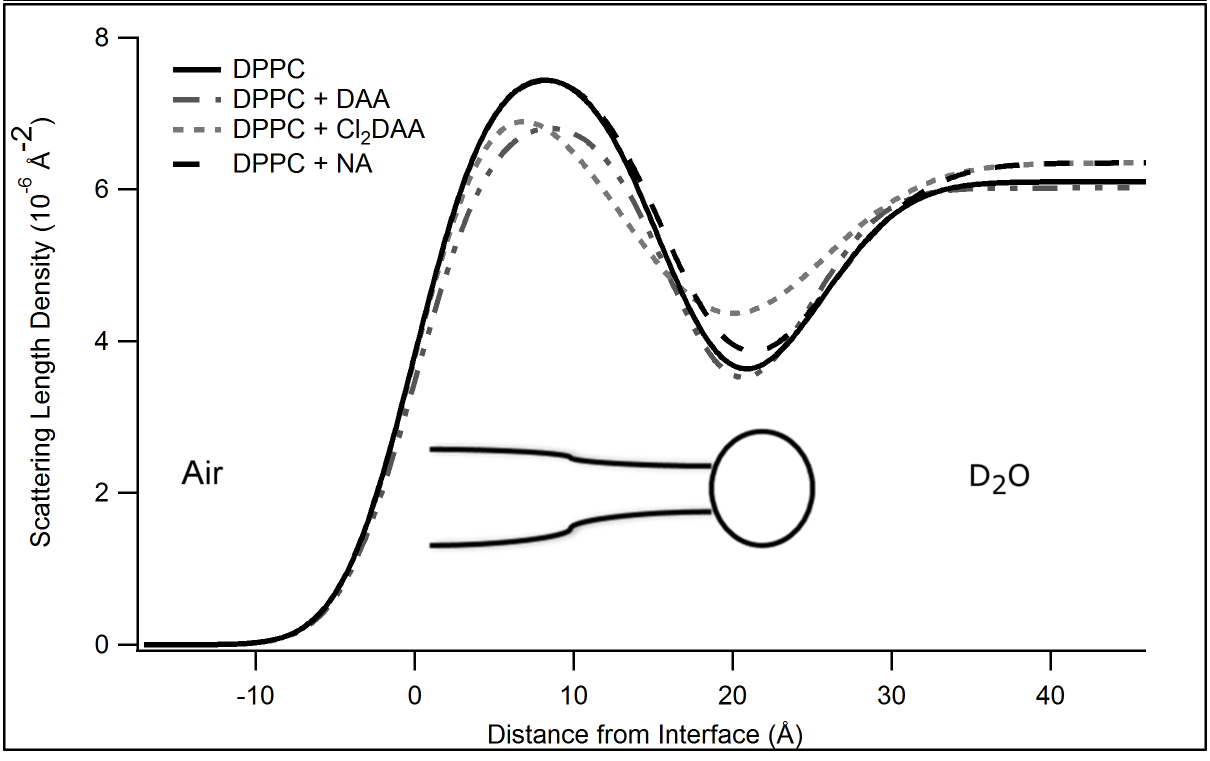
Scattering Length Density (10^-6 Å^-2)
Distance from Interface (Å)
DPPC
DPPC + DAA
DPPC + Cl2DAA
DPPC + NA
Air
D2O

DPPC
DPPC +10mol% Cl_2DAA
DPPC +10mol% DAA
DPPC +10mol% NA

15x10^3
10
5
0

enthalpy (cal/mole/°C)

20
30
40
50
60

Temperature (ºC)

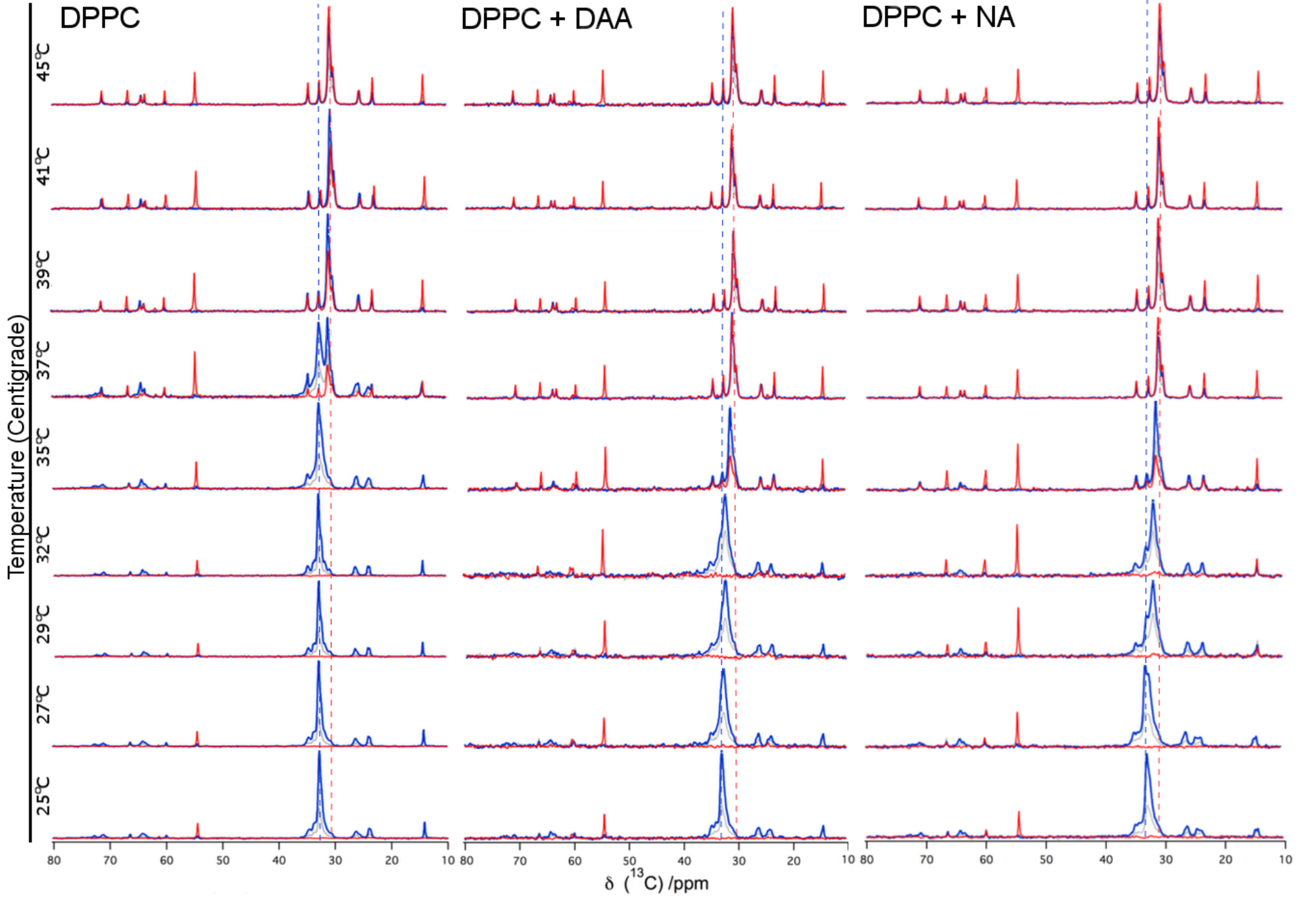
DPPC
DPPC + DAA
DPPC + NA
Temperature (Centigrade)
45℃
41℃
39℃
37℃
35℃
32℃
29℃
27℃
25℃
80 70 60 50 40 30 20 10
δ (^{13}C) /ppm

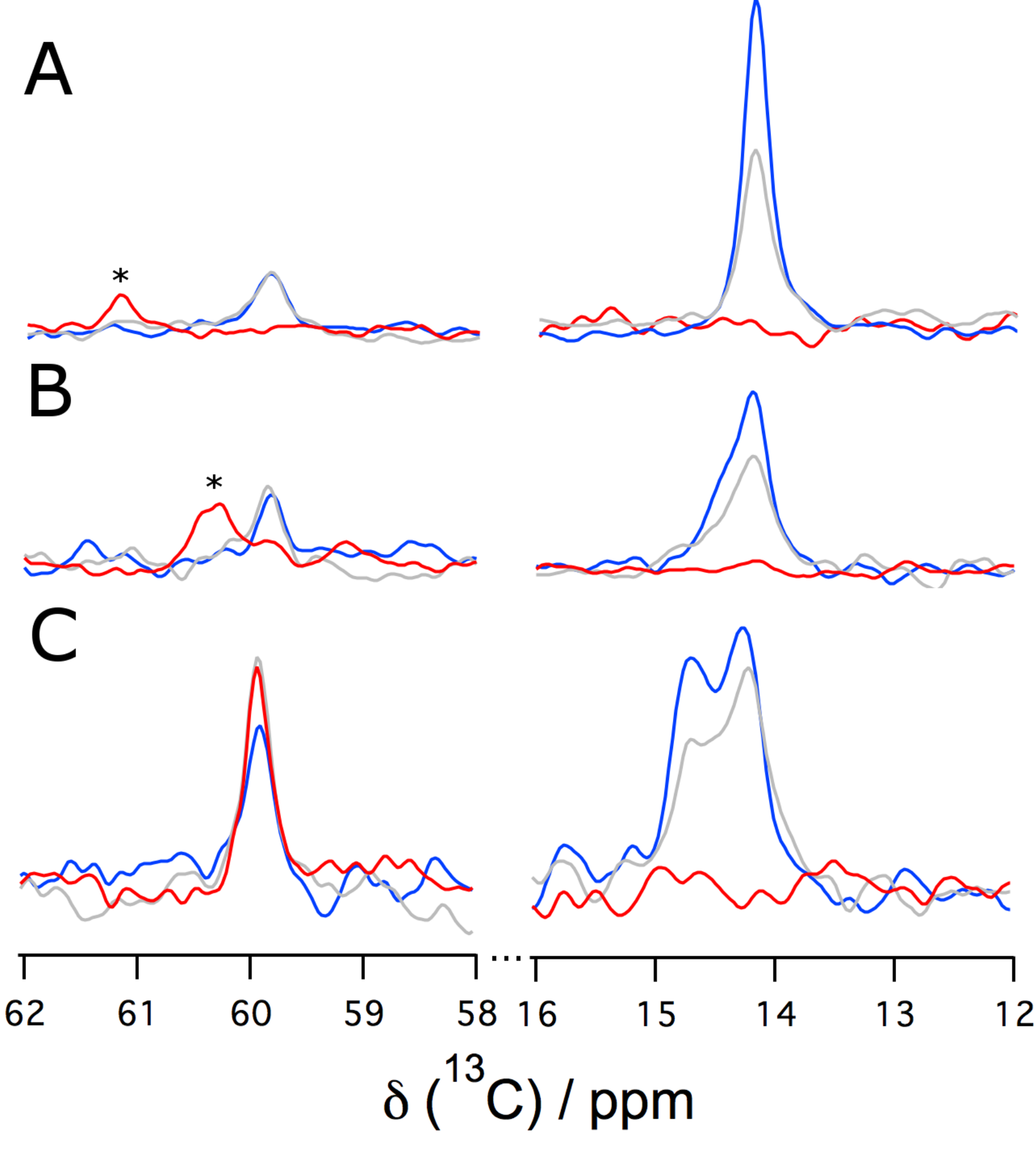
A
B
C
*
*
62
61
60
59
58
16
15
14
13
12
δ (^{13}C) / ppm

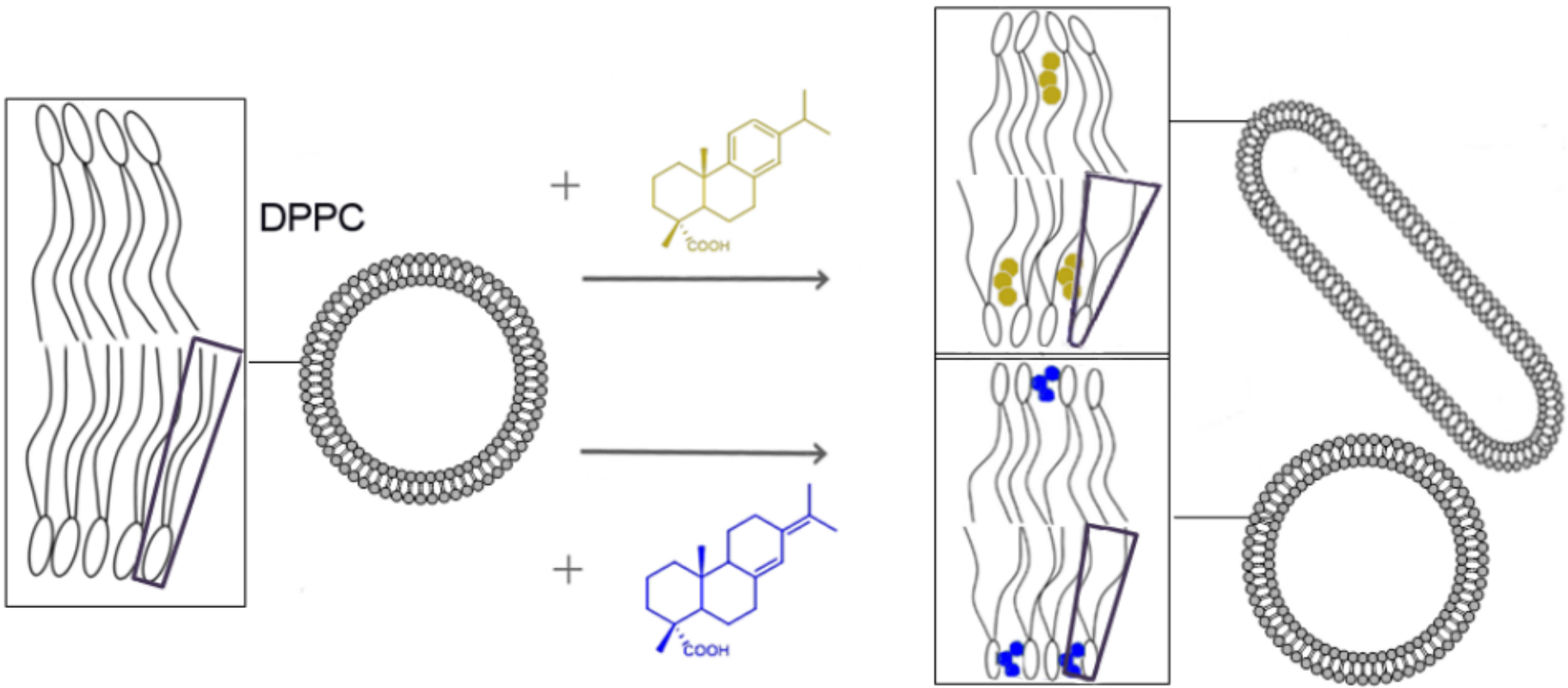
DPPC
COOH
COOH

	Tail Layer thickness (Å)	Head group Layer thickness (Å)	Roughness head/tail interface	Solvent penetration (%) head group
DPPC	16.2 ± 0.2	8.9 ± 0.5	3.7 ± 0.2	15 ± 5
DPPC/Cl_2DAA	14.7 ± 0.1	8.5± 0.3	6.0 ± 0.2	6 ± 4
DPPC/DAA	16.4 ± 0.1	7.6 ± 0.2	3.7 ± 0.2	9 ± 2
DPPC/NA	15.6 ± 0.1	9.4 ± 0.5	4.4 ± 0.1	21 ± 5

Mixture	**ΔH** (kcal/mol)	**ΔH_{vH}** (kcal/mol)	**CU**	**T_m**
DPPC	12 ± 1.0	541.2 ± 0.4	44 ± 5	41 ± 1
+ 5 mol% Cl_2DAA	13.1 ± 0.7	364 ± 1.2	27 ± 3	41 ± 1
+ 10 mol% Cl_2DAA	5.8 ± 0.5	300.0 ± 0.3	52 ± 6	40 ± 1
+ 10 mol% DAA	14 ± 2.0	241.0 ± 0.3	16 ± 3	38 ± 1
+ 10 mol% NA	18 ± 1.0	213.2 ± 0.1	12 ± 1	38 ± 1